文章编号：1001-9014(XXXX)XX-0001-12

DOI:10.11972/j.issn.1001-9014.XXXX.XX.001

# A Monolithic Integrated Medium Wave Mercury Cadmium Telluride Polarimetric Focal Plane Array

CHEN Ze-Ji, HUANG You-Wen, PU En-Xiang, XIAO Hui-Shan, XU Shi-Chun*, QIN Qiang, KONG Jin-Cheng

**Abstract**: A medium wave (MW) 640×512 (25 μm) Mercury Cadmium Telluride (HgCdTe) polarimetric focal plane array (FPA) was demonstrated. The micro-polarizer arrays (MPA) has been carefully designed in terms of line grating structure optimization and crosstalk suppression. An on-chip micro-nano fabrication process with low damage was explored, which was verified to be compatible well with HgCdTe devices. After monolithic integration of MPA, NETD < 9.5 mK was still maintained. Furthermore, to figure out the underlying mechanism that dominates extinction ratio (*ER*), specialized MPA layouts were designed, and the crosstalk was experimentally validated as the major source that impacts *ER*. By expanding opaque regions at pixel edges to 4 μm, crosstalk rates from adjacent pixels can be effectively reduced to approximately 2%, and promising *ER*s ranging from 17.32 to 27.41 were implemented.

**Key words**: Extinction ratio, infrared focal plane array, polarization, micro-polarizer array, monolithic integration

**PACS:**

# 单片集成式中波碲镉汞偏振焦平面阵列

陈泽基, 黄佑文, 浦恩祥, 肖徽山, 徐世春*, 秦 强, 孔金丞
(昆明物理研究所,云南,昆明 650223;‡. 以上作者对本工作的贡献相同)

**摘要**:提出了一种中波640×512(25 μm)的碲镉汞偏振焦平面阵列。从线栅结构优化和串扰抑制的层面,对微偏振片阵列进行了精心设计;探索了一种低损伤的片上微纳制备工艺,经验证,该工艺与碲镉汞器件兼容良好。在完成微偏振片阵列的片上集成后,NETD仍能保持在9.5 mK以下。进一步地,为揭示主导消光比的潜在作用机制,设计了特殊的微偏振片阵列排布方式,从而实验证明了串扰效应是影响消光比的主要来源。将像元边缘的遮挡区域扩展至4 μm宽,能够将来自相邻像元的串扰率有效降低至大约2%,并实现在17.32~27.41之间的优良消光比。

**关 键 词**:消光比;红外焦平面阵列;偏振;微偏振片阵列;单片集成

**中图分类号**:O43 **文献标识码**:A

## Introduction

Infrared (IR) focal plane arrays (FPA) with continually improved performance are widely used to detect the radiance intensities of target scenes[1-2]. Based on the two-dimensional spatial heat distributions, thermal imaginers distinguish the target from the background through temperature differences. However, conventional radiance intensity imaging has limited recognition capabilities in complex scenarios with interferences like clouds, dust, and tree shadows, since the target-background contrast tend to be unclear[3-5].

For this issue, infrared polarization imaging has emerged as a viable solution. As a fundamental property of light, polarization reveals more intrinsic characteristics of the imaged object, such as surface features, shapes, and roughness[6-8]. Taking advantages of distinct polarization signatures between manmade and natural objects, the target-background contrast can be effectively enhanced even under thermal equilibrium conditions.

**Foundation items**: None (This work is supported by the self-funded project of Kunming Institute of Physics).

**Biography**: CHEN Ze-Ji (1990-), male, Kunming, Ph. D. Research area involves infrared detectors, and micro-nano optoelectronic technology. E-mail: 136270894@qq.com.

* **Corresponding author**: E-mail: x.sc@163.com

The target profiles can thus be highlighted and more details can be extracted[3, 9-10]. To acquire high-quality polarimetric images, it is extremely desired to develop high-performance polarimetric IRFPAs. Mercury Cadmium Telluride (HgCdTe) is considered to be an ideal material for its superior sensitivity and quantum efficiency[2].

Among various polarimeter configurations[11], thanks to the rapid development of micro-nano technologies, micro-polarizer array (MPA) based on division-of-focal-plane (DOFP) architecture has drawn extensive attention[12-14]. With less hardware redundancy and smaller occupation, MPA enables miniaturized, integrated, and compact polarimetric imaging systems. The MPA is generally discretely or monolithically integrated with the FPA. For discrete integration, despite easier MPA fabrication process, additional bonding or gluing steps are required. Such steps increase the FPA-MPA separation, resulting in more significant diffractions. The crosstalk effects can thus be severer, which leads to reduced extinction ratios (*ER*)[15-16]. For instance, a discretely integrated medium wave (MW) 256×256 HgCdTe polarimetric FPA using gluing process exhibited moderate *ER*s around 5[17]. A long-wave (LW) 640×480 HgCdTe polarimetric FPA implemented by Indium bump bonding process possessed *ER*s less than 10[18]. For monolithic integration, with MPAs directly fabricated on the FPA surface, the diffractive crosstalks can be effectively suppressed, which enables higher performance upper limit. For example, with MPAs directly fabricated on chip, both MW and LW 256×256 HgCdTe polarimetric FPAs achieved *ER*s exceeding 10[19]. Nevertheless, it is still a bottleneck to meet the stringent process compatibility requirements posed by HgCdTe FPAs while attaining desirable performance.

In addition to integration technologies, the wave band should also be carefully selected. Compared with short wave (SW), MW and LW have significant advantages in night operation[5]. In this work, considering the manufacturing cost and technical difficulties of FPAs, the MW 640×512 (25 μm) HgCdTe FPA was chosen. The structural parameters of line gratings as well as the MPA layout have been well designed to keep the balance between the performance and fabrication feasibility. An on-chip line grating fabrication process compatible with HgCdTe FPAs was exploited. Comprehensive tests on performance of fabricated polarimetric FPAs have been conducted. In addition to performance tests, the crosstalk effect was also theoretically analyzed and experimentally characterized, which provides a better understanding about this mechanism that dominates *ER*.

## 1 Polarimetric FPA design

The schematic of the proposed monolithic integrated HgCdTe polarimetric FPA is shown in Fig. 1(a). The on-chip MPA consists of periodically distributed superpixels composed of 2×2 arranged micro-polarizers. Each pixelated micro-polarizer was formed by sub-wavelength metal line gratings. Within a superpixel, the polarization orientations of the micro-polarizers follow as a clockwise order of 0°, 45°, 90°, and 135°, respectively, as shown in Fig. 1(b). For an infrared radiation transmitting through the superpixel, its intensity is modulated by quad line gratings of different orientations, correspondingly generating four response signals: $I_0$, $I_{45}$, $I_{90}$, and $I_{135}$. Using these four measured response signals, the Stokes parameters of the incoming radiation can be calculated via the following equations [20]:

$$S_0 = \frac{1}{2}\left(I_0 + I_{90}\right), S_1 = I_0 - I_{90}, S_2 = I_{45} - I_{135}. \quad (1)$$

The degree of linear polarization (*DOLP*) as well as the angle of polarization (*AOP*) can thus be calculated via the following equations:

$$DOLP = \frac{\sqrt{S_1^2 + S_2^2}}{S_0}, AOP = \frac{1}{2}\arctan\left(\frac{S_2}{S_1}\right), \quad (2)$$

It should be noted that the relationship between the calculated and the actual *DOLP* values takes the form as[21]:

$$DOLP = \frac{ER - 1}{ER + 1} DOLP_{act}, \quad (3)$$

where $DOLP_{act}$ denotes the actual *DOLP*. Clearly, the higher the *ER*, the more accurate the measured *DOLP*. For this purpose, a finite-different time-domain (FDTD) model was established to provide guidance on line grating optimizations. The boundary conditions as well as the meshing size have been properly set.

The structural parameters of line gratings, i. e., thickness, period, and duty cycle, were initially set as 300 nm, 800 nm, and 50%, respectively. The variation tendencies of *ER* with respect to a certain parameter were simulated with the other twos maintained unchanged. As can be seen from Fig. 2(a), as thickness increases, *ER* tends to be higher. However, too thick line gratings are not practical, since the re-deposition effect existing in the etching process can be detrimental to *ER* as well as the transverse magnetic (TM) wave transmittance. Fig. 2(b) illustrates that *ER* increases with the reduced grating period, nevertheless, an excessively shrunk grating period will pose a challenge to the fabrication process. Regarding Fig. 2(c), it can be inferred that *ER* rises rapidly with an improved grating duty cycle, however, simply improving the duty cycle can degrade the TM transmittance. To keep the balance between the process feasibility and polarization selectivity, the thickness ranging from 300 nm to 500 nm and period from 600 to 800 nm are suggested, while the duty cycle is kept as 50%.

It should be addressed that the above-mentioned model corresponds to an ideal case that the line gratings are infinitely distributed, wherein the crosstalk has not been involved. Nevertheless, for pixelated micro-polarizers, the distributed areas of line gratings are limited. Therefore, the crosstalks are nonnegligible, which results in significant *ER* reductions[16]. The crosstalk mechanisms can be categorized as two types: optical and electrical[21]. The optical crosstalk can be attributed to the misalignment and/or diffraction. For the former one, if a micro-polarizer spans two pixels due to the MPA-FPA misalignment, the crosstalk occurs. The misalignment

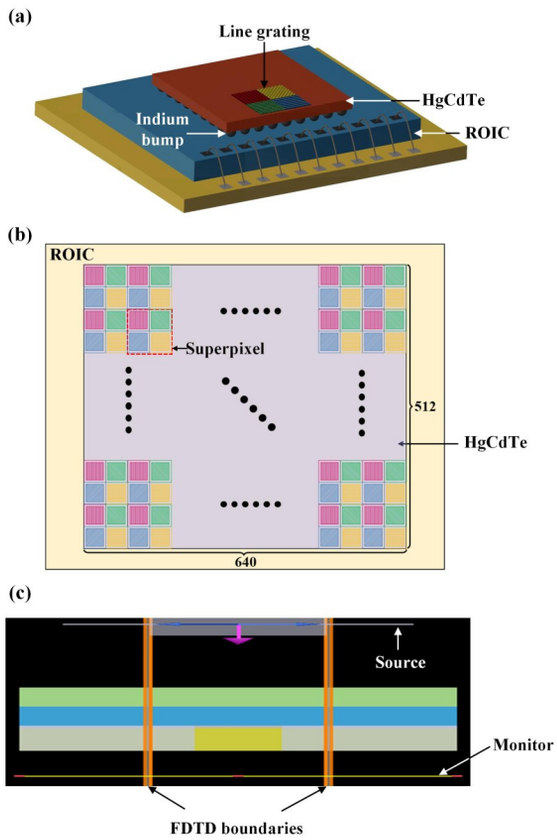


Fig. 1 (a) The schematic of a monolithic polarimetric FPA. (b) The arrangement of superpixels. (c) The established model to optimize structural parameter.
图 1 (a)单片集成式焦平面阵列示意图;(b)超像元排布;(c)所建用于结构参数优化的模型

induced crosstalk can be effectively avoided by improving the alignment precision and setting opaque regions at the pixel edges. Regarding diffraction induced crosstalk, it appears when radiation diffracts through the micro-polarizer aperture. The radiation propagates through the MPA-FPA separation, and ultimately impinges adjacent pixels[21]. Obviously, this kind of crosstalk tends to be more pronounced when the MPA-FPA separation increases[16]. In our previous work, with the entire superpixel modeled, the variation tendency of *ER* with respect to the MPA-FPA separation has been clarified[22]. With MPA directly fabricated on the FPA, the crosstalks caused by diffractions can be effectively suppressed.

The electrical crosstalk can be attributed to photo-generated carriers migrating from one pixel to the adjacent ones. When the opaque regions at the pixel edges are expanded, the photo-generated carriers can be confined within the pixel central regions, thereby alleviating electrical crosstalks.

Although expanding opaque regions is effective for suppressing both optical and electrical crosstalks, this method could result in severe transmittance degradation. Therefore, trade-off is necessary. Herein two types of MPA layouts with different configurations of opaque regions are designed, as shown in Fig. 3. The first one, referring as MPA layout A, follows as the design reported in our previous work, wherein the vertical and horizontal micro-polarizers have wider opaque regions than the diagonal ones. When the opaque region widths are the same, due to the inconstant line grating lengths, the diagonally oriented pixels have inferior polarization selectivity. Therefore, the opaque regions widths of differently oriented micro-polarizers were modified to balance *ER*s of differently oriented pixels. Another design refers as MPA layout B. Regardless of micro-polarizer orientations, the widths of the opaque regions were all set as 4 μm to suppress crosstalks. To compensate for the reduced photosensitive area, the period of line gratings was properly scaled down. This design aimed at verifying if enlarging opaque regions is beneficial for *ER* enhancements at the expense of limited transmittance reduction. The structural parameters of these two MPA layouts are listed in Table 1.

## 2 On-chip MPA fabrication process

A simple and low-damage on-chip process was exploited to directly fabricate MPA on the MW640×512 (25 μm) HgCdTe FPA (Fig. 4(a)) surface. The FPAs have been previously tested and the qualified ones were selected for subsequent process.

Firstly, a 20 nm thick Ti layer and a 400 nm thick Au layer were successively deposited on the FPA by e-beam evaporation, serving as the structural layers (Fig. 4(b)). The Ti layer was employed to enhance the adhesion between the Au layer and the FPA. Subsequently, the MPA was patterned using laser direct writing process (Fig. 4(c)) and etched using ion-beam milling process (Fig. 4(d)).

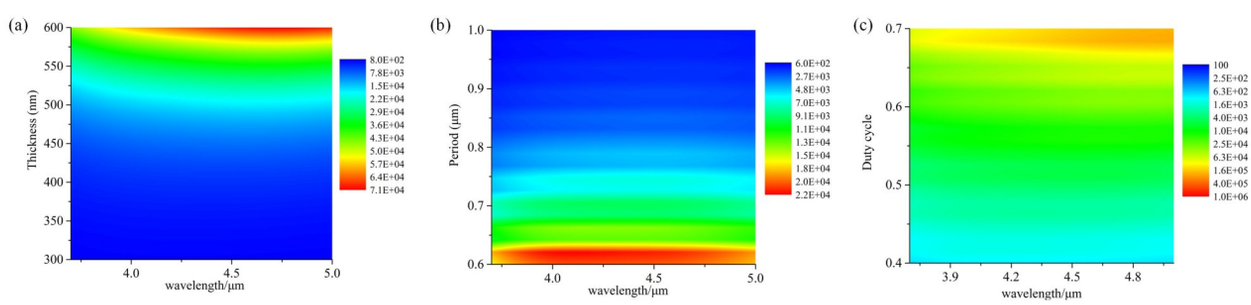


Fig. 2 *ER* variation tendencies with respect to different structural parameters: (a) thickness, (b) period, and (c) duty cycle.
图2 消光比随不同结构参数的变化趋势:(a)厚度,(b)周期,以及(c)占空比。

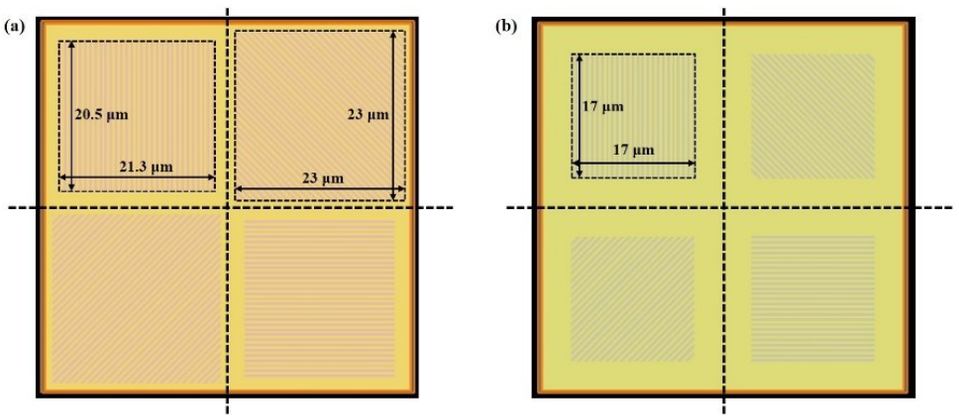


Fig. 3 Superpixels with layouts of previously reported design (a), and expanded opaque regions (b).
图 3 超像元版图:(a)早期设计,(b)遮挡区域扩展。

**Table 1 Structural parameters of MPA layout A and B**
**表 1 微偏振片阵列版图 A 和版图 B 的结构参数**

| | Thickness (nm) | Period (nm) | Duty cycle |
|---|---|---|---|
| MPA layout A | 400 | 700 | 50% |
| MPA layout B | 400 | 600 | 50% |

During the deposition, the temperature of HgCdTe FPA should be strictly controlled below 80 °C. The e-beam evaporation, magnetic sputtering, and ion beam sputtering processes can all meet this requirement. All the Ti/Au layers attained by these three types of processes remain intact during the entire process flow. Given that keeping continuities of lithographic pattern lines is extremely important for attaining expected *ER*s, the qualities of metal layers were evaluated from the perspective of roughness. As can be clearly seen from Fig. 5, the e-beam evaporation allows for Au layers with minimal roughness, which is selected as a preferable deposition technique in this work.

For sub-wavelength line gratings, the lithography process is a crucial step which determines if the performance of the fabricated MPA addresses expectations. Herein the maskless laser direct writing technique was employed to achieve both flexible MPA layout modifications and line width down to 300 nm. The laser intensity as well as the focal length are two critical parameters. To search out the optimal process condition, a two-dimensional test matrix was employed in this work. Within the matrix, each "element" had the same pattern involving a group of line grating arrays with different duty cycles and line widths, whereas each row and column corresponded to a different laser intensity and focal length, respectively. Therefore, various combinations of exposure parameters together with their corresponding exposure effects were obtained. Consequently, the optimal parameters were determined, and the corresponding MPA pattern is given in Fig. 6. Another key indicator of lithography refers as misalignment, which could be a nonnegligible source of crosstalk. By properly designing the alignment mark and carefully calibrating the equipment, misalignment down to ±1 μm has been realized, which can be totally covered by the opaque regions at the pixel edges. Therefore, the misalignment caused crosstalks can be effectively suppressed.

Regarding etching, ion milling featuring ion bombardment is a physical dry etching process, making it appropriate for etching multi-layer metals[23]. It is should be noted that the particles of target materials are sput-

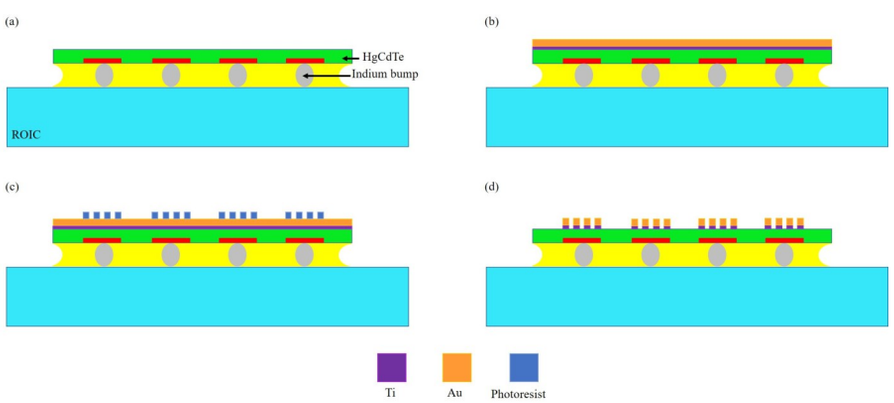


Fig. 4 A MW640×512 (25 μm) HgCdTe FPA (a) based on-chip process: (b) Ti/Au depositions, (c) laser direct writing, and (d) iron-beam milling.
图 4 基于中波 640×512(25 μm)焦平面探测器阵列(a)的片上工艺:(b)Ti/Au沉积;(c)激光直写;(d)离子铣刻蚀

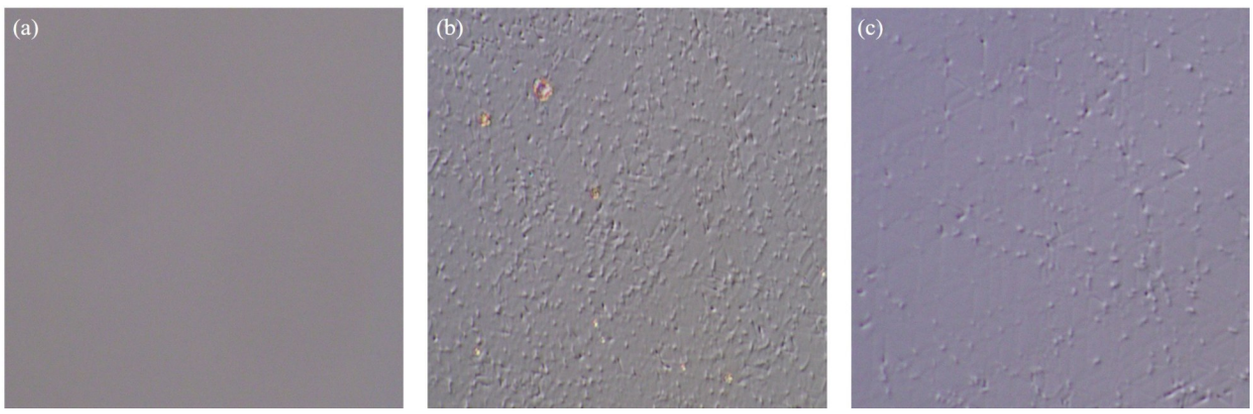


Fig. 5 Surface morphologies of Au layers fabricated by: (a) e-beam evaporation, (b) magnetic sputtering, and (c) ion beam sputtering.
图 5 不同工艺制备的Au层表面形貌:(a)电子束蒸发;(b)磁控溅射;(c)离子束溅射

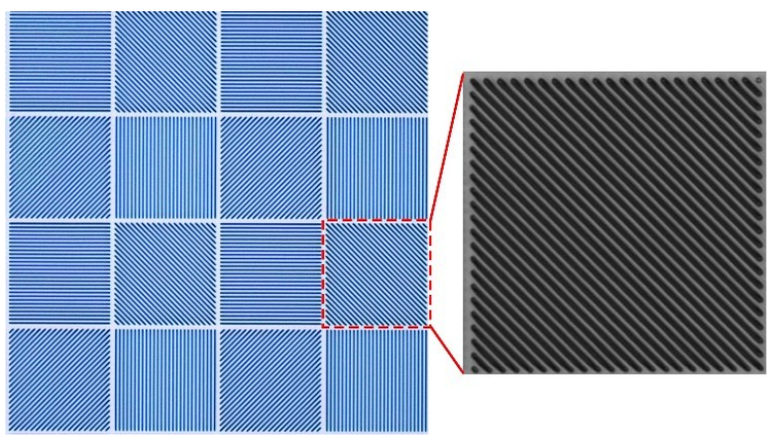

Fig. 6 Patterned line gratings with optimal process parameters of laser direct writing.
图 6 采用最佳激光直写工艺参数所得线栅图案

tered at different angles under ion bombardment[23]. The sputtered particles with large angles relative to the normal direction tend to redeposit onto the sidewalls of the readily etched patterns. This redeposition is deleterious to the etching profile, especially for subwavelength structures[24]. As can be seen from the cross-sectional profile shown in Fig. 7(a), with process conditions generally used for micrometer-scale patterns, i. e., normal incident of ion beam, low acceleration voltage, and high ion density, strong redeposition effect occurred and the line grating gaps were nearly filled up. To solve this issue, modifications such as increasing the incident angle of ion beam, raising the acceleration voltage, and reducing the ion density have been carried out, which greatly alleviated the redeposition effect, as shown in Fig. 7(b).

图 7线栅的横截面形貌:(a)工艺条件调整前;(b)工艺条件调整后。

To sum up, thru a series of optimizations for the process flow, low-damage MPA fabrication on the FPA surface has been implemented. Fig. 8 gives the scanning electron microscope (SEM) photographs of the fabricated MPA.

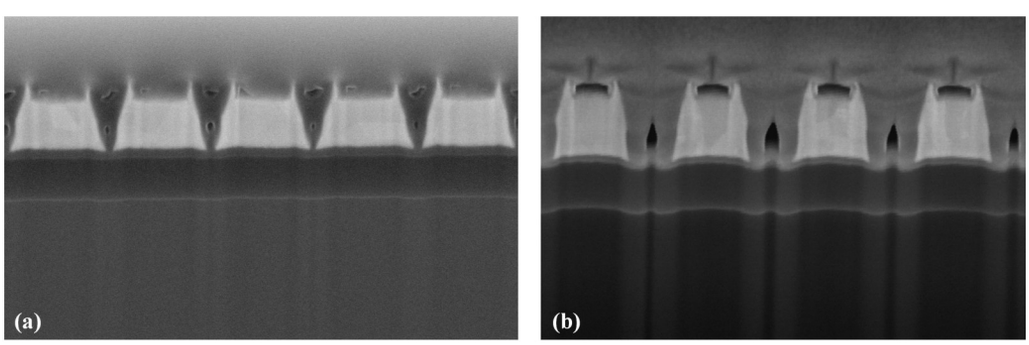


Fig. 7 Cross-sectional profiles of etched line gratings (a) before and after (b) process condition modifications.

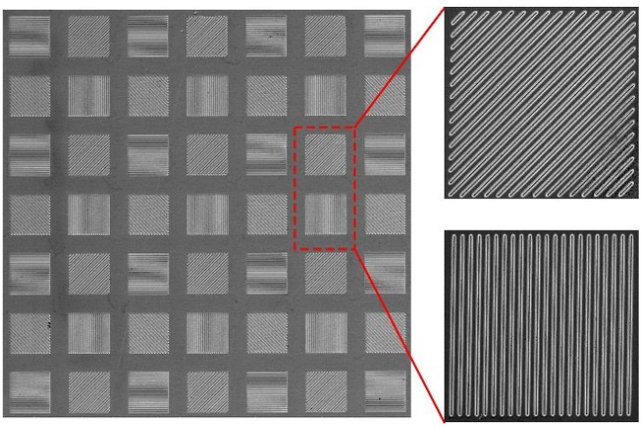

Fig. 8 SEM photographs of monolithically fabricated MPA.
图 8 片上制备的微偏振片阵列SEM照片

## 3 Results and discussions

### 3.1 Test setup establishment

The performance of polarimetric FPA assemblies was characterized using the test setup as shown in Fig. 9. The black body served as a source of signal irradiation. The rotational polarizer with *ER* over 500 was utilized to modulate the unpolarized irradiation as the polarized one with various polarization angles. A customized test printed circuit board (PCB) was connected to the electrical interface of the assembly. The measured data can thus be transferred to the computer so that the performance indicators can be extracted.

### 3.2 Radiometric performance characterization

The fabricated polarimetric FPAs with MPA layout A and B were encapsulated in standard test Dewars. The radiometric performance of polarimetric FPAs was firstly measured. In this case, the polarizer was not needed. For both two types of polarimetric FPAs, pursuant to GB/T 17444-2013, the tests were performed at the liquid nitrogen temperature under the half-well integration capability filling condition, wherein the background and target temperatures were set as 293 K and 308 K, respectively. For both two types of polarimetric FPAs, the measured data before and after monolithic integration were summarized in Table 2.

In ideal conditions, after MPA fabrication, the integration time should be twice as long as that before, since half of the unpolarized radiance intensities are reflected by the line gratings. However, due to limited line grating distribution areas together with the fabrication tolerances, there exists acceptable divergencies between the measured integration time and the ideal one. In addition, after MPA fabrication, the integration time of B-type polarimetric FPA only slightly extended compared to that of the A-type one, indicating that the loss of radiance intensities led by enlarged opaque regions was not severe.

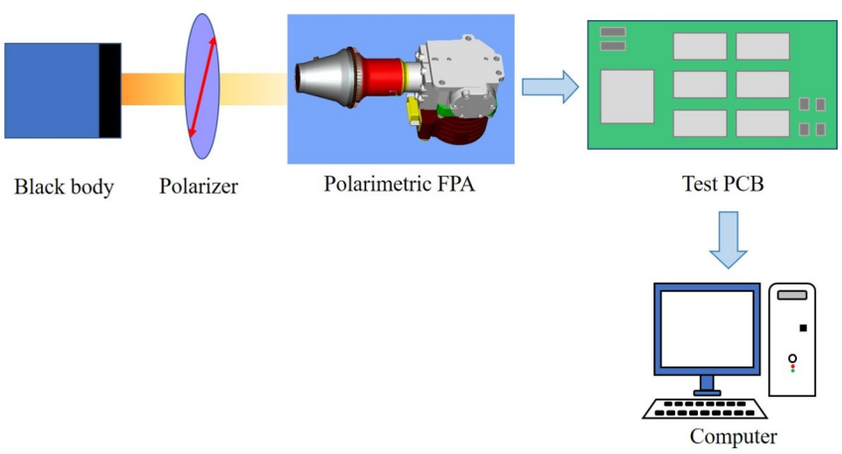


Fig. 9 Test setup of the polarimetric FPA.
图 9 偏振焦平面探测器阵列的测试平台

**Table 2 Radiometric performance of two types of polarimetric FPAs before and after MPA fabrication (fab.)**
**表 2 微偏振片阵列制备前后,两类偏振焦平面探测器阵列的辐射性能**

| | Polarimetric FPA type A | | Polarimetric FPA type B | |
|---|---|---|---|---|
| | Before MPA fab. | After MPA fab. | Before MPA fab. | After MPA fab. |
| Integration time (ms) | 3.1 | 5.2 | 3.2 | 5.9 |
| Response signal (mV) | 814 | 964 | 826 | 777 |
| Peak detectivity (cm·Hz$^{1/2}$/W) | $1.64\times10^{11}$ | $1.51\times10^{11}$ | $1.84\times10^{11}$ | $1.24\times10^{11}$ |
| Noise (mV) | 0.534 | 0.535 | 0.480 | 0.490 |
| NETD (mK) | 9.86 | 8.39 | 8.72 | 9.49 |
| Nonuniformity (%) | 5.32 | 11.31 | 4.53 | 8.88 |
| Effective pixel rate (%) | 99.981 | 95.875 | 99.758 | 96.191 |

After MPA fabrication, the response signal and noise did not worsen, indicating that the FPA damage induced by the process was controllable. According to GB/T 17444-2013, the peak detectivity can be determined via[25]:

$$D_p^* = G\frac{1}{M\cdot N-(d+h)}\sum_{i=1}^{M}\sum_{j=1}^{N}\sqrt{\frac{A_D}{2\tau}}\frac{R(i,j)}{V_N(i,j)}, \tag{4}$$

where $G$ is the spectral factor, $M$ and $N$ refer to the FPA rows and columns, $d$ and $h$ refer to the dead and overheat pixels, and the sum of $d$ and $h$ represents the total blind pixels of the FPA. $A_D$ and $\tau$ denote the pixel area as well as half-well integration time. $V_N(i, j)$ represents the noise of a certain pixel, and $R(i, j)$ referred as the responsivity can be calculated using the following formulas[25]:

$$R(i,j) = \frac{V_S(i,j)}{P}, \tag{5}$$

$$P = \frac{\sigma(T_2^4 - T_1^4)A_D}{4F^{\#2}+1}, \tag{6}$$

where $V_S(i, j)$ denotes the response signal of a certain pixel, $\sigma$ refers to the Stepan's constant, $T_2$ and $T_1$ are the target and background temperatures, respectively. According to Eqns. (4-6), after MPA fabrication, the peak detectivity is supposed to reduce due to the increased integration time. The measured results were in accordance with the theoretical analysis.

Regarding NETD, it takes the form as[25]:

$$NETD = \frac{1}{M\cdot N-(d+h)}\sum_{i=1}^{M}\sum_{j=1}^{N}\frac{T_2-T_1}{V_S(i,j)/V_N(i,j)}. \tag{7}$$

Similarly, the NETD variation tendencies can be obtained according to the response signals and noises before and after MPA fabrication. For both two types of polarimetric FPAs, the measured and theoretically analyzed results were consistent.

What's more, the increased response nonuniformities for both two types of polarimetric FPAs can be mainly attributed to the ion beam etching. To improve the uniformity, the key point is to have a nearly maintained etch rate in both central and peripheral regions of the FPA. As for effective pixel rate, upon blind pixel distribution diagrams as given in Fig. 10, for both two types of polarimetric FPAs, most blind pixels were concentrated on the FPA edges. Such a phenomenon is caused by the thick photoresist accumulated there. Faced with this issue, we have made some preliminary attempts, including modifying the spin-coating parameters of the photoresist and increasing the laser intensities at the FPA edges. With blind pixels remarkably reduced, the effective pixel rate has raised up to 98.23%, as shown in Fig. 11. To have more substantial progress, further research is ongoing.

Above all, despite enlarged opaque regions, by taking appropriate compensation strategies such as reducing the line grating period, B-type polarimetric FPA exhibited comparable radiometric performance as the A-type one.

### 3.3 Extinction ratio extraction

With polarizer incorporated into the test setup, the response signals under different polarizer rotation angles can be attained. The strongest and weakest signals, generated by the TM and TE incidents, are referred as $V_{TM}$ and $V_{TE}$, respectively. The $ER$ can thus be determined via the following equation:

$$ER = \frac{V_{TM}}{V_{TE}}. \tag{8}$$

For both two types of polarimetric FPAs, the polarization response curves of differently oriented pixels were plotted in Figs. 12 and 13, respectively. The extracted $ER$s were listed in Table 3. Sinusoidal fittings have been carried out, which inferred that the measured data matched well with Malus' Law. It is evident that B-type polarimetric FPA possessed significantly higher $ER$s than those of the A-type one. It is worth mentioning that for B-type polarimetric FPA, the $ER$ of 0°-oriented pixels was 7.26, which was lower than those of pixels with other orientations. It was found that the cycle duty of 0°-oriented line gratings was slightly reduced, which could result from the nonuniformities induced by laser direct writing process.

In regards to the B-type polarimetric FPA, we have further optimized the entire MPA fabrication process and have formally encapsulated it in the standard metal micro-Dewar. As shown in Fig. 14, the measured $ER$s ranged from 17.32 to 27.41, which were greatly enhanced compared to those measured in the test Dewar. This phenomenon was caused by different transmittance ranges between the test and formal Dewars. For the test Dewar, due to the absence of optical filter, the transmittance

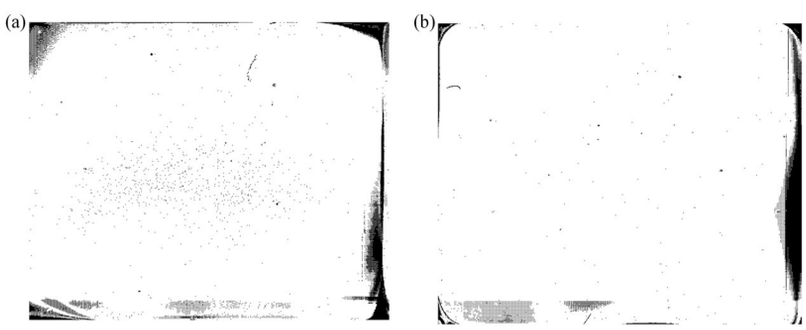


Fig. 10 Blind pixel distribution diagrams of (a) A-type and (b) B-type polarimetric FPAs.
图 10 偏振焦平面阵列的盲元分布图:(a)A型和(b)B型

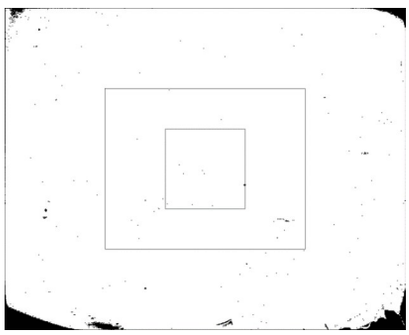

Fig. 11 Blind pixel distribution diagram of polarimetric FPA after preliminary process optimization.
图 11 初步优化工艺后,偏振焦平面阵列的盲元分布图

range was 1~5 μm. For incident lights with shorter wavelengths, the line gratings should be shrunk to the corresponding subwavelength scale to ensure sufficient polarization selectivity. However, regarding described MPA designed for 3.7~4.8 μm, the line grating period was too large for shorter wavelengths, thereby leading to inadequate polarization selectivity. Consequently, the overall *ER*s dropped down. By contrast, for the formal Dewar, the optical filter was involved, and the transmittance range of 3.7~4.8 μm matched well with the designed

**Table 3 *ER*s of two types of polarimetric FPAs**
**表 3 两类偏振焦平面阵列的消光比**

| | *ER* | | | |
|---|---|---|---|---|
| | 0° | 45° | 90° | 135° |
| A-type polarimetric FPA | 5.41 | 5.08 | 4.92 | 5.19 |
| B-type polarimetric FPA | 7.26 | 9.17 | 9.28 | 9.52 |

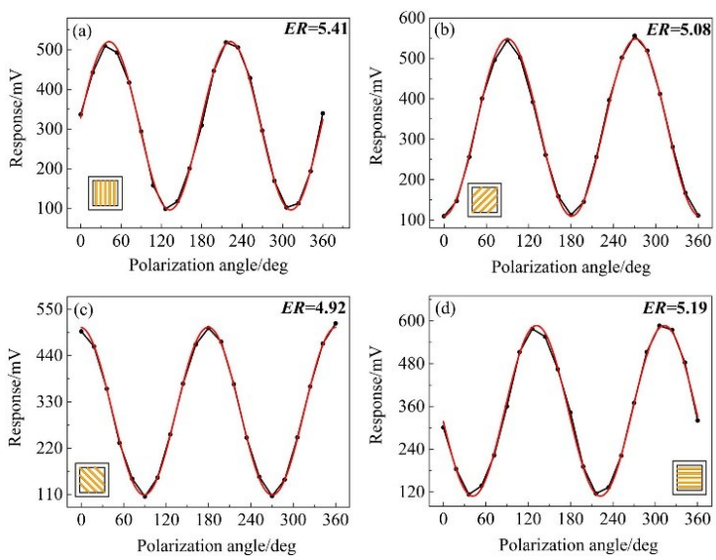


Fig. 12 Polarization response curves of pixels with 0°, 45°, 90°, and 135° (a-d) orientations for A-type polarimetric FPA.
图 12 对于A型偏振焦平面阵列,0°、45°、90°和135°(a-d)取向像元的偏振响应曲线。

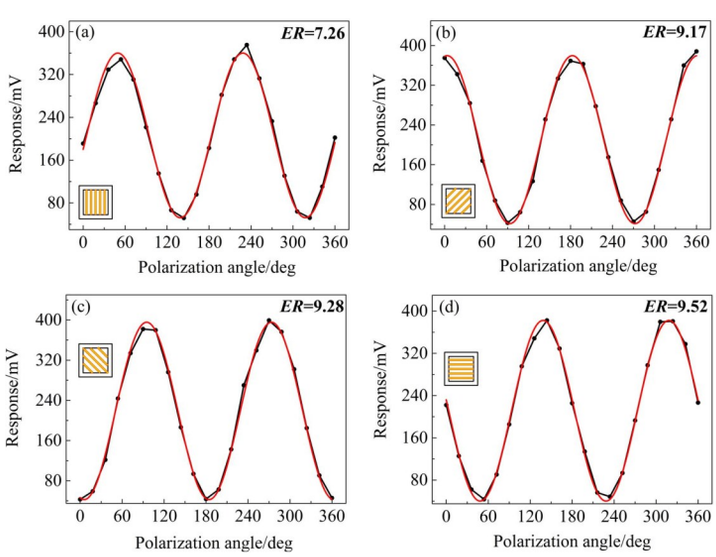


Fig. 13 Polarization response curves of pixels with 0°, 45°, 90°, and 135°orientations (a-d) for B-type polarimetric FPA.
图 13 对于B型偏振焦平面阵列,0°、45°、90°和135°取向(a-d)像元的偏振响应曲线。

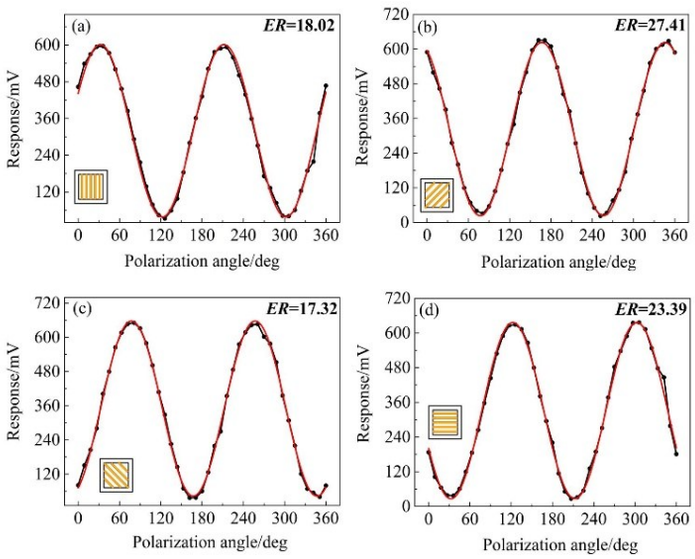


Fig. 14 Polarization response curves of pixels with 0°, 45°, 90°, and 135° orientations (a-d) for formally encapsulated B-type polarimetric FPA.
图 14 正式封装后,B型偏振焦平面阵列0°、45°、90°和135°取向(a-d)像元的偏振响应曲线。

MPA, thus achieving higher *ER*s. Table 4 compared the described polarimetric FPA with the reported ones. The performance of this work is superior.

Above all, it has been experimentally validated that expanding opaque regions at the pixel edges is an effective methodology to improve *ER*s while maintaining promising radiometric performance. The differences among *ER*s of pixels with various orientations indicate that the uniformity of the MPA is still needed to be improved, which will be a key focus in the future work.

### 3.4 Crosstalk rate determination

It is critical to have an insight into the dominant mechanism that limits *ER* so that further optimizations can be conducted to make greater performance breakthroughs. To figure out whether it is the crosstalk that leads to significant *ER* differences between two types of polarimetric FPAs, specialized MPA layouts have been designed to quantitatively characterize the crosstalk rates from adjacent pixels.

For instance, as shown in Fig. 15(a), the 0°-oriented pixels were all covered by the Au layer. For these pixels, the signals generated by external radiations have been eliminated, and the measured ones are mostly contributed by crosstalks from adjacent pixels. For pixels with other orientations, the crosstalk signals from their adjacent pixels can also be extracted using the similar layout designs.

The signal response of the pixel oriented in a certain polarization angle can be expressed as[27]:

**Table 4 Performance comparison among this work and the reported ones**
**表 4 已报道工作和本工作性能对比**

| | References | | | |
|---|---|---|---|---|
| | [19] | [26] | [17] | This work |
| Array size | 256×256(30 μm) | 1024×1024(25 μm) | 256×256(30 μm) | 640×512(25 μm) |
| NETD (mK) | Not given | Not given | Not given | 9.49 |
| *ER* | >10 | Not given, expected to be over 10 | ~5 | 17.32~27.41 |

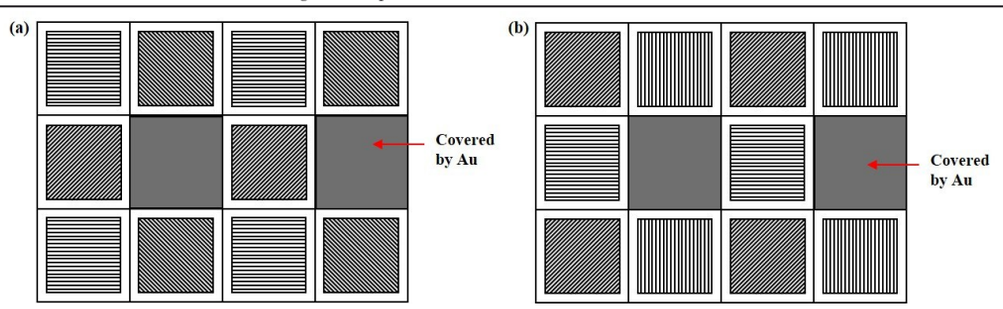


Fig. 15 Specialized MPA layout to determine crosstalk rates from adjacent pixels of (a) 0°- and (b) 45°-oriented pixels.
图 15 特殊的微偏振片阵列版图,用于确定(a)0°取向偏振单元和(b)45°取向偏振单元的相邻像元串扰率。

$$\begin{aligned}
V_0 &= \frac{1}{2}(1-P)(q_1+r_1)V_{p1} + P\left(q_1\sin^2(0-\alpha)+r_1\cos^2(0-\alpha)\right)V_{p1}\\
V_{45} &= \frac{1}{2}(1-P)(q_2+r_2)V_{p2} + P\left(q_2\sin^2\left(\frac{\pi}{4}-\alpha\right)+r_2\cos^2\left(\frac{\pi}{4}-\alpha\right)\right)V_{p2}\\
V_{90} &= \frac{1}{2}(1-P)(q_3+r_3)V_{p3} + P\left(q_3\sin^2\left(\frac{\pi}{2}-\alpha\right)+r_3\cos^2\left(\frac{\pi}{2}-\alpha\right)\right)V_{p3}\\
V_{135} &= \frac{1}{2}(1-P)(q_4+r_4)V_{p4} + P\left(q_4\sin^2\left(\frac{3\pi}{4}-\alpha\right)+r_4\cos^2\left(\frac{3\pi}{4}-\alpha\right)\right)V_{p4}
\end{aligned}, \tag{9}$$

where $P$ denotes the degree of polarization for the polarizer, $V_{pi}$ ($i$=1, …, 4) represent the response signal of the corresponding pixel before MPA fabrication, $q_i$ and $r_i$ ($i$=1, …, 4) refer to TM and TE transmittances, respectively, $\alpha$ is the polarization angle of the incident light. In this equation, $\frac{1}{2}(1-P)(q_i+r_i)V_{pi}$ represents the response signal generated by the unpolarized portion of the incident lights transmitted through the polarizer, and $P\left(q_i\sin^2(\theta-\alpha)+r_i\cos^2(\theta-\alpha)\right)V_{pi}$, $\theta$ = 0, $\frac{\pi}{4}$, $\frac{\pi}{2}$, $\frac{3\pi}{4}$ represents the response signal generated by the polarized portion of the incident lights transmitted through the polarizer.

Taking the 0° -oriented pixels an example, when these pixels were covered, the measured crosstalk signals from the adjacent pixels can be written as:

$$\begin{aligned}
V_{c1} &= 2\left(\frac{1}{2}(1-P)(q_2+r_2)V_{p2} + P\left(q_2\sin^2\left(\frac{\pi}{4}-\alpha\right)+r_2\cos^2\left(\frac{\pi}{4}-\alpha\right)\right)V_{p2}\right)\chi\\
&+2\left(\frac{1}{2}(1-P)(q_4+r_4)V_{p4} + P\left(q_4\sin^2\left(\frac{3\pi}{4}-\alpha\right)+r_4\cos^2\left(\frac{3\pi}{4}-\alpha\right)\right)V_{p4}\right)\chi
\end{aligned}, \tag{10}$$

where $\chi$ denotes the crosstalk rate. In Eqn. (10), the former and latter terms represent crosstalk signals contributed by the left and right 45°-oriented pixels, and upper and lower 135° -oriented pixels, respectively. The weak crosstalks from diagonal pixels were neglected. In ideal conditions, $V_{p2}$ and $V_{p4}$, $q_2$ and $q_4$, $r_2$ and $r_4$ are equivalent, therefore, Eqn. (10) can be simplified as:

$$V_{c1} = 2(q_2+r_2)V_{p2}\chi. \tag{11}$$

In this case, the sum of crosstalk signals from adjacent pixels is a constant independent of the polarization angle.

However, the measured signals of the covered pixels appeared as sinusoidal curves, as shown in Fig. 16 (a). The discrepancies between experimental results and theoretical analysis can be ascribed to the response nonuniformities existed in the FPA as well as the polarization nonuniformities induced by the MPA. Such nonuniformities have led to different $V_{pi}$, $q_i$, and $r_i$ values. In this case, as per Eqn. (10), the crosstalk signals sinusoidally varied with the polarization angle. The sum of the response signals from adjacent pixels was also plotted in Fig. 16(a). After fitting these two curves, it can be observed that their phases and periods were consistent. By calculating the ratio of these two groups of data, the crosstalk rate of 3.48% can be determined. Since both 0°- and 90°-oriented pixels are surrounded by two pairs of perpendicularly oriented pixels (45° and 135°), the depicted calculation process for 0° -oriented pixels is equivalent for 90° -oriented ones. Therefore, the crosstalk rate from adjacent pixels of the 90° -oriented ones was also 3.48%. As for 45°/135° -oriented pixels, the MPA layout as shown in Fig. 15(b) was utilized. With the similar approach, the measured and fitted results as shown in Fig. 16(b) were acquired, by which the crosstalk rate was determined as 4.54%.

For B-type polarimetric FPA, the same methods were adopted. Based on the measured data and fitted curves as shown in Fig. 17, the crosstalk rates from adja-

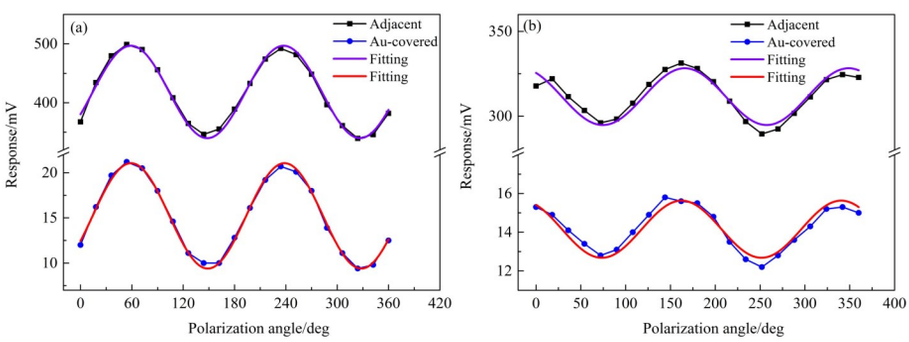


Fig. 16 Measured data used to determine the crosstalk rates from adjacent pixels of (a) 0°/90°- and (b) 45°/135°-oriented pixels for A-type polarimetric FPA.

图 16 测试数据:对于A型偏振焦平面阵列的(a) 0°/90°和(b) 45°/135°取向像元,用于确定来自其相邻像元的串扰率

cent pixels of 0°/90°- and 45°/135°-oriented pixels were calculated to be 1.70% and 2.06%, respectively.

For A-type polarimetric FPA, when the crosstalk signals imposed with TE response signals were detracted, as shown in Fig. 18, the *ER*s of 0°- and 45°-oriented pixels recovered to 16.37 and 17.94, respectively. For B-type polarimetric FPA, using the same method, the *ER*s of 0°- and 45°-oriented pixels recovered to 17.22 and 25.97, respectively. Obviously, for both two types of polarimetric FPAs, the re-extracted *ER*s became closer, strongly inferring that it was the distinct crosstalk rates that led to significant *ER* differences. As previously discussed, the lithography misalignment of ±1 μm can be covered by the opaque regions. With MPA directly fabricated on the FPA surface, the diffraction induced crosstalks have been suppressed. Therefore, the optical crosstalks have been essentially minimized. It is reasonable to believe that the electrical crosstalk is the mechanism that dominates *ER*. Furthermore, it should be noted that after re-extractions, there still exists noticeable *ER* differences between the 45°-oriented pixels for two types of polarimetric FPAs. This could be caused by process tolerances among different fabrication batches.

Above all, expanding opaque regions up to 4 μm can effectively reduce the crosstalk rate by more than half. Even so, simultaneously setting all the opaque region widths as 4 μm could still be a preliminary design. For pixels with various orientations, it would be a more flexible method to accordingly expand their opaque regions to different extents, which is expected to implement more balanced and desirable *ER*s.

## 4 Conclusions

In summary, this work developed a monolithic integrated MW HgCdTe polarimetric FPA with remarkable radiometric performance and polarization selectivity. A complete flow including design, fabrication, and test was comprehensively described, which would be beneficial for facilitating the practical applications of HgCdTe polarimetric FPAs.

At design stage, systematical optimization for MPA layout has been carried out. Not only the structural parameters of line gratings, but also the crosstalks have been considered.

The feasibility and compatibility of proposed monolithic MPA fabrication process have been demonstrated, which achieved favorable *ER*s ranging from 17.32 to 27.41. More efforts on improving non-uniformity will be taken.

The crosstalk mechanism has been deeply discussed, which provided a helpful guidance on MPA designs. It was verified that properly expanding opaque regions implemented substantial *ER* enhancements at the cost of very limited radiometric performance scarifica-

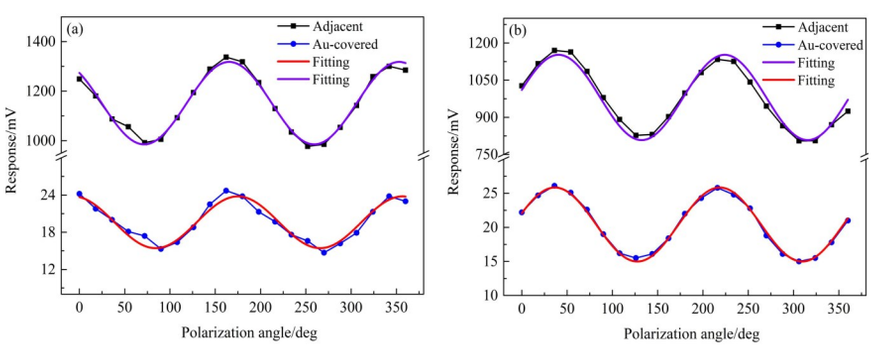


Fig. 17 Measured data used to determine the crosstalk rates from adjacent pixels of (a) 0°/90°- and (b) 45°/135°-oriented pixels for B-type polarimetric FPA.
图 17 测试数据:对于B型偏振焦平面阵列的(a) 0°/90°和(b) 45°/135°取向像元,用于确定来自其相邻像元的串扰率

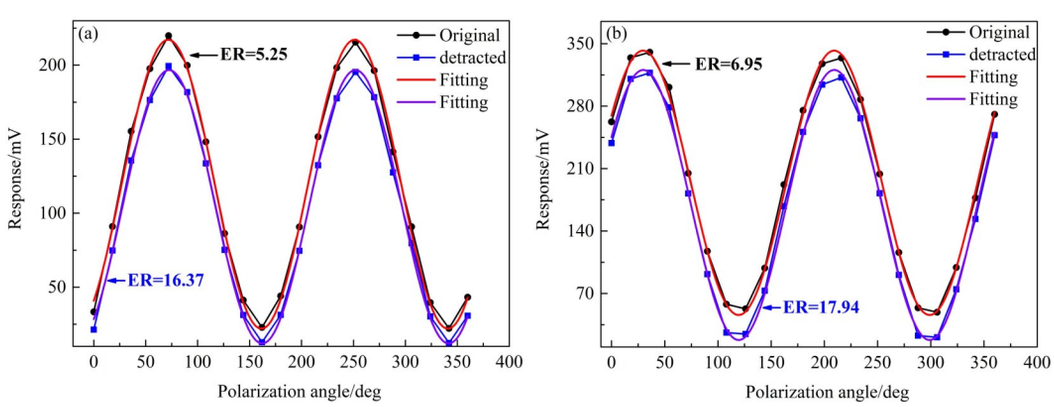


Fig. 18 Re-extracted *ER*s of (a) 0°- and (b) 45°-oriented pixels for A-type polarimetric FPA.
图 18 A型偏振焦平面阵列中,(a) 0°和(b) 45°像元的重提取消光比。

tion. With more flexible opaque region settings, the overall performance of the proposed polarimetric FPA is expected to be preferrable.

## Acknowledgment

The authors would like to express their heartfelt gratitude to LI Yong-Liang, ZHAO Gui-Qin, TANG Jin-Chun, SHU Chang, YIN Hui, WEI Hong, LIN Zhan-Wen, and other staff for their kind help throughout the fabrication process.

## References

[1] Rogalski A, Martyniuk P, Kopytko M. Challenges of small-pixel infrared detectors: a review [J]. *Reports on Progress in Physics*, 2016, **79**(4): 046501.
[2] Bhan R, Dhar V. Recent infrared detector technologies, applications, trends and development of HgCdTe based cooled infrared focal plane arrays and their characterization [J]. *Opto-Electronics Review*, 2019, **27**(2): 174-193.
[3] Felton M, Gurton K, Pezzaniti J, Chenault D, Roth L. Comparison of the inversion periods for MidIR and LWIR polarimetric and conventional thermal imagery [C]//Polarization: Measurement, Analysis, and Remote Sensing IX. SPIE, 7672: 198-208.
[4] HAO Zhai, LUO Xiao-Lin, JIANG Zhao-Zhen, HU Zheng-Hao. Infrared polarization detection method for weak target in sky background [C]//AOPC 2020: Optical Sensing and Imaging Technology. SPIE, 11567: 212-221.
[5] Tyo J S, Goldstein D L, Chenault D B, Shaw J A. Review of passive imaging polarimetry for remote sensing applications [J]. *Applied Optics*, 2006, **45**(22): 5453-5469.
[6] Hong S. Surface roughness and polarization ratio in microwave remote sensing [J]. *International Journal of Remote Sensing*, 2010, **31**(10): 2709-2716.
[7] Beamer D, Abeywickrema U, Banerjee P. Polarization vector signatures for target identification [C]//Polarization Science and Remote Sensing VIII. SPIE, 10407: 208-214.
[8] Sun D, Li T, Yang B, Shao X, Li X, Chen Y. Research on polarization performance of InGaAs focal plane array integrated with super-pixel-structured subwavelength grating [J]. *Optics express*, 2019, **27**(7): 9447-9458.
[9] Felton M, Gurton K, Pezzaniti J, Chenault D, Roth L. Measured comparison of the crossover periods for mid-and long-wave IR (MWIR and LWIR) polarimetric and conventional thermal imagery [J]. *Optics express*, 2010, **18**(15): 15704-15713.
[10] Chenault D B, Pezzaniti J L, Vaden J P. Pyxis handheld polarimetric imager [C]//Infrared Technology and Applications XLII. SPIE, 9819: 158-168.
[11] Bieszczad G, Gogler S, Świderski J. Review of design and signal processing of polarimetric imaging cameras [J]. *Opto-Electronics Review*, 2021, **29**
[12] Andreou A G, Kalaylian Z K. Polarization imaging: principles and integrated polarimeters [J]. *IEEE Sensors journal*, 2002, **2**(6): 566-576.
[13] WU Zhi, Powers P E, Sarangan A M, ZHAN Qi-Wen. Optical characterization of linegrid micropolarizers designed for infrared imaging polarimetry [J]. 2008, **33**(15): 1653-1655.
[14] Lemaster D A, Hirakawa K. Improved microgrid arrangement for integrated imaging polarimeters [J]. *Optics Letters*, 2014, **39**(7): 1811-1814.
[15] Cruz-Cabrera A, Kemme S, Wendt J, Boye R, Carter T, Samora S. Polarimetric imaging cross talk effects from glue separation between FPA and micropolarizer arrays at the MWIR [C]//Photonics Packaging, Integration, and Interconnects VII. SPIE, 6478: 252-264.
[16] Vorobiev D, Ninkov Z, Gartley M. Polarization in a snap: imaging polarimetry with micropolarizer arrays [C]//Polarization: Measurement, Analysis, and Remote Sensing XI. SPIE, 9099: 13-27.
[17] YANG Chao-Wei, FENG Yuan-Qing, LI Dong-Sheng, *et al*. Preparation of medium wave mercury cadmium telluride infrared polarization focal plane detector (Invited) [J]. Infrared and Laser Engineering, 2021, **50**(1): 20211008.(杨超伟, 封远庆, 李东升, 等. 中波碲镉汞红外偏振焦平面探测器的制备研究(特邀) [J]. **红外与激光工程**). 2021, **50**(1): 20211008.
[18] Hubbs J E, Gramer M E, Maestas-Jepson D, *et al*. Measurement of the radiometric and polarization characteristics of a microgrid polarizer infrared focal plane array [C]//Infrared Detectors and Focal Plane Arrays VIII. SPIE, 6295: 71-83.
[19] Malone N R, Hampp A, Gordon E E, *et al*. Detection comparisons between LWIR and MWIR polarimetric sensors [C]//Polarization: Measurement, Analysis, and Remote Sensing VIII. SPIE, 6972: 197-205.
[20] Yongqiang Z, Wuteng L, Seong G K, Yong L, Quan P. Design and performance analysis of infrared micro-polarizer array [C]//2015 34th Chinese Control Conference (CCC). IEEE: 4574-4580.
[21] Jones M W, Persons C M. Performance predictions for micro-polarizer array imaging polarimeters [C]//Polarization Science and Remote Sensing III. SPIE, 6682: 51-61.
[22] CHEN Ze-Ji, XIAO Hui-Shan, XU Shi-Chun, PU EN-Xiang, *et al*. Study on micropolarizer array performance dependences on assembling process [C]//Ninth Symposium on Novel Photoelectronic Detection Technology and Applications. SPIE, 12617: 1305-1310.
[23] Smith R, Makh S, Walls J. Surface morphology during ion etching The influence of redeposition [J]. *Philosophical Magazine A*, 1983, **47**(4): 453-481.
[24] Moreno-Marin J, Valles-Abarca J, Gras-Marti A. Secondary effects in ion milling [J]. *Journal of Vacuum Science Technology B: Microelectronics Processing and Phenomena*, 1986, **4**(1): 322-325.
[25] GB/T 17444-2013, Measuring methods for parameters of infrared focal plane arrays [S]. CN-GB, 2013(GB/T 17444-2013, 红外焦平面阵列参数测试方法 [S]. 国家市场监督管理总局 CN-GB, 2013
[26] Forrai D P, Endres D W, Devitt J W, *et al*. Development of a MWIR polarimetric FPA [C]//Infrared Systems and Photoelectronic Technology II. SPIE, 6660: 54-63.
[27] HUANG Fei, LI Fan-Ming, CHEN Wei-Cong, ZHANG Rui, *et al*. Calibration method for division of focal plane polarimeters [J]. *Applied optics*, 2018, **57**(18): 4992-4996.